Observations of parity nonconservation in atomic thallium

P. H. Bucksbaum, E. D. Commins, and L. R. Hunter
Physics Department, University of California, Berkeley, California 94720
and Materials and Molecular Research Division, Lawrence Berkeley Laboratory, Berkeley, California 94720
(Received 26 January 1981; revised manuscript received 26 May 1981)

A detailed account is given of observations of parity nonconservation in the $6\,^2P_{1/2}$-$7\,^2P_{1/2}$ transition in $^{203,205}_{81}$Tl. Absorption of circularly polarized 293-nm photons by $6\,^2P_{1/2}$ atoms in an E field results in polarization of the $7\,^2P_{1/2}$ state through interference of the Stark $E1$ amplitude with $M1$ and parity-nonconserving $E1$ amplitudes. This polarization is detected by selective excitation of $m_F = \pm 1$ components of the $7\,^2P_{1/2}$ state to the $8\,^2S_{1/2}$ state and observation of the ensuing decay fluorescence at 323 nm. Systematic corrections due to imperfect circular polarization, misaligned E fields, and residual magnetic fields are determined precisely by a series of auxiliary experiments. The result is expressed in terms of the circular dichroism $\delta_{\text{expt}} = +(2.8^{+1.0}_{-0.9})\times 10^{-3}$, to be compared with estimates based on the Weinberg-Salam model for $\sin^2\theta_w = 0.23$: $\delta_{\text{theo}} = +(2.1\pm 0.7)\times 10^{-3}$.

I. INTRODUCTION

In this paper we report observations of parity nonconservation in the $6\,^2P_{1/2}$-$7\,^2P_{1/2}$ transition in atomic thallium ($Z = 81$, $A = 203, 205$). This effect occurs because of the neutral weak interaction between valence electron and nucleus, and its observation provides a useful test of the Weinberg-Salam (standard) model of weak and electromagnetic interactions.[1-6] Parity nonconservation in the electron-nucleon interaction has also been observed in scattering of high-energy polarized electrons on deuterium[7,8] and in a number of optical-rotation experiments in atomic bismuth.[9-12]

The results of a preliminary version of the present experiment,[13] and more recently a brief summary of our latest results,[14] have already been published. Here we present a detailed description of the experimental apparatus and procedure, an analysis of systematic errors and corrections, a summary of results and a comparison with theory and other experiments.

It is generally assumed that the neutral weak interaction between electron (e) and nucleon (N) occurs by exchange of a massive neutral vector boson Z^0. This exchange modifies the Coulomb Hamiltonian by adding an effective zero-range potential H' containing scalar (S) and pseudoscalar (P) parts: $H' = H_S + H_P$. Assuming the standard model, the dominant contribution to H_P is

$$H_W = \frac{G}{2\sqrt{2}} Q_W \rho(\vec{r}) \gamma_5 , \tag{1}$$

where G is the Fermi coupling constant, $Q_W = (1 - 4\sin^2\theta_W) Z - N$, and $\rho(\vec{r})$ is the nuclear density, $\vec{r}$ being the electron position.[3-6] Matrix elements of H_W are nonzero only for atomic orbitals of opposite parity with nonvanishing value or gradient at the nucleus ($s_{1/2}$, $p_{1/2}$ orbitals), and these matrix elements vary approximately as Z^3.

The transition $6\,^2P_{1/2}$-$7\,^2P_{1/2}$ in Tl (see Fig. 1) is forbidden $M1$ with measured amplitude[15]

$$\mathfrak{M} = (-2.1\pm 0.3)\times 10^{-5} \left| \frac{e\hbar}{2m_e c} \right| . \tag{2}$$

Parity nonconservation causes the $6\,^2P_{1/2}$, $7\,^2P_{1/2}$ states to be admixed with $^2S_{1/2}$ states and the transition amplitude acquires an electric dipole component $\mathcal{E}_p$, given to order G by

$$\mathcal{E}_p = \sum_{n\,^2S_{1/2}} \left(\frac{\langle 7\,^2P_{1/2} | O_{\text{EM}} | nS\rangle \langle nS | H_W | 6\,^2P_{1/2}\rangle}{E_{6P_{1/2}} - E_{nS}} + \frac{\langle 7\,^2P_{1/2} | H_W | nS\rangle \langle nS | O_{\text{EM}} | 6\,^2P_{1/2}\rangle}{E_{7P_{1/2}} - E_{nS}} \right), \tag{3}$$

where O_{EM} is the $E1$ electromagnetic transition operator. Interference between $\mathcal{E}_p$ and $\mathfrak{M}$ results

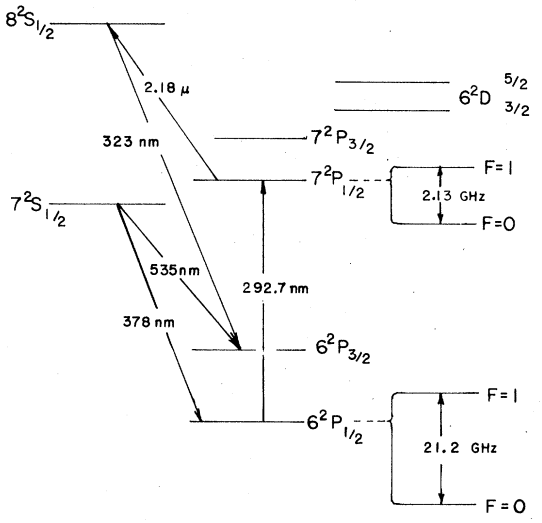

FIG. 1. Low-lying energy levels of Tl (not to scale).

in circular dichroism, defined by

$$\delta=\frac{\sigma_+-\sigma_-}{\sigma_++\sigma_-}=\frac{2\,\mathrm{Im}(\mathfrak{M}\mathcal{E}_p)}{|\mathfrak{M}|^2+|\mathcal{E}_p|^2}\approx\frac{2\,\mathrm{Im}\mathcal{E}_p}{\mathfrak{M}}\,, \tag{4}$$

where $\sigma_\pm$ are the cross sections for resonant absorption of 293-nm circularly polarized photons with $\pm$ helicity, respectively. (Time-reversal invariance requires $\mathcal{E}_p$ and $\mathfrak{M}$ to be relatively imaginary.[4]) Theoretical estimates of $\mathcal{E}_p$ and δ have been carried out by a number of authors.[5,16,17] The wave functions generated in some of these calculations[17] have been used to compute various auxiliary quantities for comparison with spectroscopic data. In general, agreement between calculation and experiment for these quantities is very satisfactory. From Ref. 17 one obtains the following theoretical predictions for $\sin^2\theta_W=0.23$:

$$\mathcal{E}_{p,\mathrm{theo}}=-2.26\times10^{-8}i\,|\mu_B|\,, \tag{5a}$$

$$\delta_{\mathrm{theo}}=\frac{2\,\mathrm{Im}(\mathcal{E}_{p,\mathrm{theo}})}{\mathfrak{M}_{\mathrm{expt}}}=+2.1\times10^{-3}. \tag{5b}$$

Recently, more sophisticated many-body calculations of $\mathcal{E}_p$ have been carried out, yielding a similar result.[18]

II. EXPERIMENTAL METHOD

We employ a method first suggested by Bouchiat and Bouchiat,[4] in which an external electric field E is applied to Tl vapor. This field mixes, by the Stark effect, $^2P_{1/2}$ states with $^2S_{1/2}$ and $^2D_{3/2}$ states. The $6P_{1/2}$-$7P_{1/2}$ transition intensity, proportional to E^2, is thus increased above background (the latter being due to light scattering and atom-atom collisions). Interference between $\mathfrak{M}$ and the Stark amplitude, and between $\mathcal{E}_p$ and the Stark amplitude, results in an angular momentum polarization of the $7\,^2P_{1/2}$ state. Let the 293-nm (UV) photon beam be along $\hat{x}$ and choose $\vec{E}=E\hat{y}$ [see Fig. 2(a)]. One then finds the $7\,^2P_{1/2}$ polarization along $\hat{z}$ to be

$$P_z(F=0\to F'=1)\simeq-\frac{2\mathfrak{M}}{\beta E}(1\pm\delta/2)\,, \tag{6}$$

$$P_z(F=1\to F'=1)\simeq\frac{(4\alpha-2\beta)\mathfrak{M}}{(3\alpha^2+2\beta^2)E}(1\pm\delta/2)\,, \tag{7}$$

$$P_z(F=0\to F'=0)=0 \tag{8}$$

for each indicated hyperfine-splitting (hfs) component $6\,^2P_{1/2}$, $F\to7\,^2P_{1/2}$, F' of the transition.[19] Here $\pm$ refer to $\pm$ 293-nm-photon helicities. Also αE, βE are Stark amplitudes, with

$$\alpha=\tfrac{1}{9}\sum_{nS}R_{7P,nS}R_{6P,nS}\left(\frac{1}{E_7-E_{nS}}+\frac{1}{E_6-E_{nS}}\right)\cdot$$
$$+\tfrac{2}{9}\sum_{nD_{3/2}}R_{7P,nD}R_{6P,nD}\left(\frac{1}{E_7-E_{nD}}+\frac{1}{E_6-E_{nD}}\right), \tag{9}$$

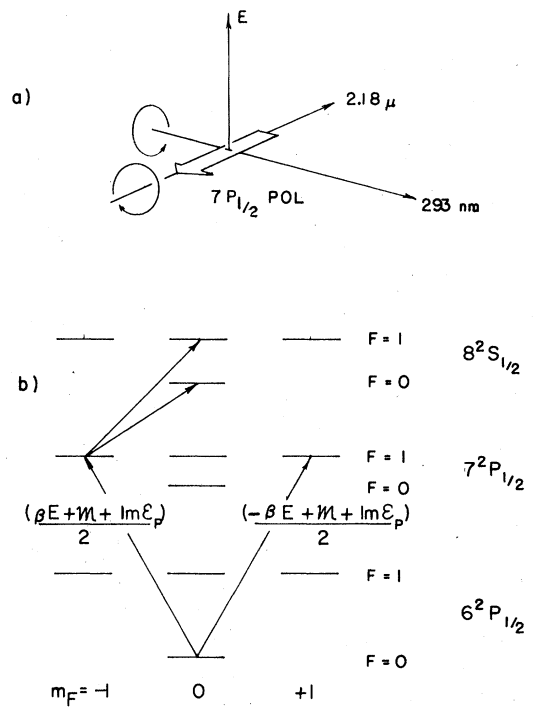

FIG. 2. (a) Orientation of electric field, polarization, and wave vectors in the experiment. (b) Schematic diagram of energy levels (not to scale), illustrating production of polarization in the $7\,^2P_{1/2}$ state, $F=0\to F'=1$ transition, and analysis of polarization by selective excitation to the $8\,^2S_{1/2}$ state. The amplitudes for the transitions $6\,^2P_{1/2}$, $F=0$, $m_F=0\to7\,^2P_{1/2}$, $F=1$, $m_F=\pm1$ are shown.

$$\beta=\tfrac{1}{9}\sum_{nS}R_{7P,nS}R_{6P,nS}\left(\frac{1}{E_6-E_{nS}}-\frac{1}{E_7-E_{nS}}\right)$$
$$+\tfrac{1}{9}\sum_{nD_{3/2}}R_{7P,nD}R_{6P,nD}\left(\frac{1}{E_7-E_{nD}}-\frac{1}{E_6-E_{nD}}\right), \tag{10}$$

where $E_6=E(6\,^2P_{1/2})$, $E_7=E(7\,^2P_{1/2})$, and $R_{7P,nS}=\langle7\,^2P_{1/2}|r|n\,^2S_{1/2}\rangle$, etc. The parity-nonconserving terms in the polarization [i.e., those proportional to $\frac{1}{2}\delta$ in Eqs. (6) and (7)] are pseudoscalars of the general form $h\,\mathbf{k}\times\vec{\mathbf{E}}\cdot\langle\vec{\mathbf{F}}\rangle$, where h is the photon helicity, $\vec{\mathbf{k}}$ is the photon wave vector, and $\vec{\mathbf{F}}$ is the atomic angular momentum in the $7\,^2P_{1/2}$ state.

We analyze the $7\,^2P_{1/2}$ polarization by selective excitation of the $m_F=+1$ or -1 components of this state to the $8\,^2S_{1/2}$ state, using circularly polarized 2.18-μm light, directed along $-z$, and we observe the intensity of 323-nm ($8\,^2S_{1/2}$-$6\,^2P_{3/2}$) fluorescence [see Fig. 2(b)]. The analyzing power of this method is measured to be 0.70 ± 0.07. Figure 3 is a schematic diagram of the apparatus, which we now describe in detail.

The cell consists of a "main" section which en-

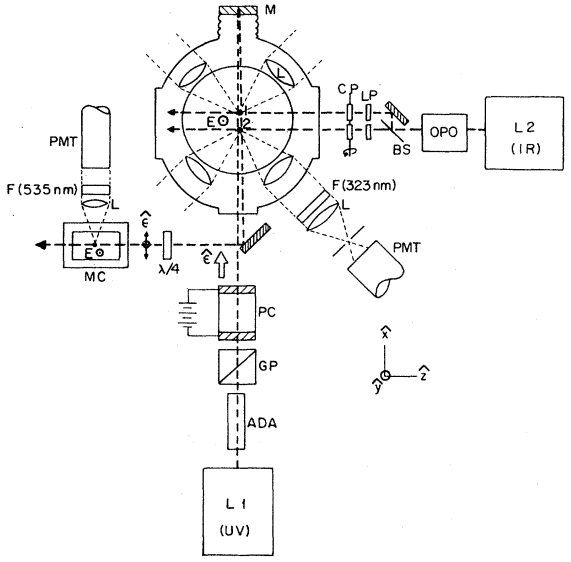

FIG. 3. Schematic diagram of apparatus. L1, L2: Flashlamp pumped pulsed dye lasers; ADA: Doubling crystal; GP: Glan-air polarizing prism; PC: Pockels cell for production of circularly polarized 293-nm light; OPO: Optical parametric oscillator for production of 2.18-μm light; BS: Beam splitter; LP: linear polarizers for 2.18-μm light; CP: Circular polarizers; E: Electric field; L: Fused-quartz lenses; LF: Liquid filter; F: Interference filters; M: Retroreflecting mirror; MC: Monitor cell.

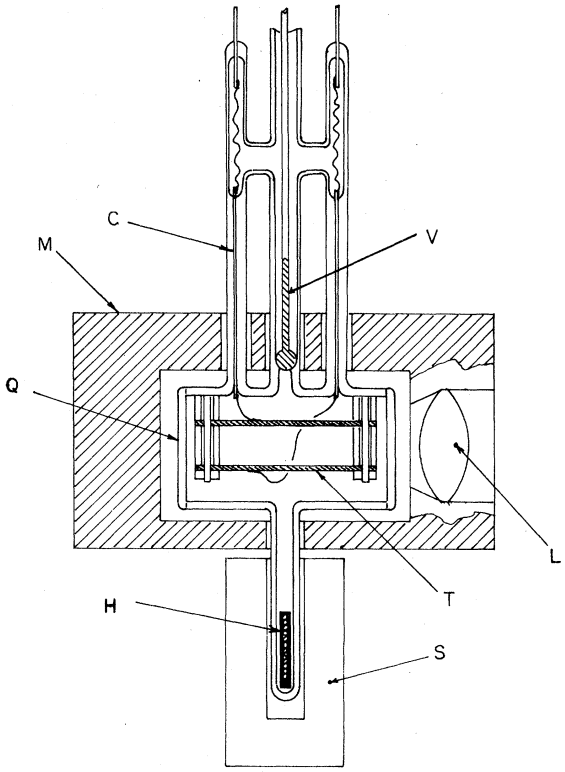

FIG. 4. Cell and ovens. V: quartz ball valve and lifter; C: capillary tubes; M: main oven; Q: cylindrical cell wall; T: tantalum electrodes; L: lens; S: stem oven; H: tantalum crucible with thallium load.

closes the electric field region, and a "stem" section, the thallium reservoir. These are constructed of fused quartz, and are supported by a pumpout tube which is normally kept closed by means of a remotely actuated ground quartz ball-and-socket valve. Surrounding the cell are the "main" and "stem" ovens, which are electrically heated stainless steel (see Fig. 4). The cell body consists of a suprasil cylinder (Amersil Corp.) of 69-mm outside diameter 2-mm wall thickness, fused to top and bottom fused quartz end-plates. The cylinder was carefully selected for high optical quality. The electrodes are flat tantalum plates of 1-mm thickness, suspended from the cell ceiling by quartz rods and spacers. The electrode separation is 14 mm. The connecting tantalum wires pass through closely fitting quartz capillary tubes to tungsten-glass feedthroughs in the cold portion of the cell assembly. Thallium condenses in the capillaries and seals them.

The stem is a 5-mm-outside-diameter quartz tube below the main body of the cell. It contains a tantalum crucible which is loaded with 99.999% pure thallium metal with the natural isotopic abundances (29.5% ^{203}Tl, 70.5% ^{205}Tl). During the experiment the stem temperature is maintained at about 920 °K (corresponding to a Tl vapor density $n \simeq 10^{15}$ cm^{-3}) and the main portion of the cell is at about 1000 °K. The cell-oven assembly is surrounded by three concentric cylindrical stainless-steel heat shields and mounted inside a rough vacuum tank. The pressure in the latter is deliberately maintained at about 5×10^{-3} Torr with a controlled air leak so that oven surfaces remain oxidized. This minimizes the presence of chromium and/or manganese vapor which attacks quartz at 1000 °K.

The experiment employs two essentially identical flash-lamp pumped tunable pulsed dye lasers ($L1$, $L2$), built in this laboratory. Details of design and construction have been reported elsewhere.[20] $L1$ operates at 585 nm and is used to produce 293-nm light in a doubling crystal for the $6\,^2P_{1/2}$-$7\,^2P_{1/2}$ transition. The pulse is 0.5 μs full width at half maximum (FWHM) and approximately 1 GHz in bandwidth. The frequency is actively stabilized by computer control of intracavity optics. Typical output energy is 10-12 mJ/pulse at a repetition rate of 20 s^{-1}. Laser $L2$ delivers 6–7 mJ/pulse with a bandwidth of approximately 15 GHz. The two lasers are synchronized and

have a relative time jitter of less than 5 ns.

Light from $L1$ is focused with an $f=62$ cm lens into a $0.5\times0.5\times5.0$ cm crystal of $NH_4H_2AsO_4$ (ADA) for second-harmonic generation. The crystal is temperature stabilized to maintain a 90° phase match condition. Typically we generate 0.6–0.7 mJ/pulse at 293 nm. Light emerging from the ADA crystal is linearly polarized vertically, orthogonal to the 585-nm pump beam. A Glan-air calcite prism is used to separate the beams and define the UV linear polarization precisely before the beam enters the circular polarizer. The latter is a Pockels cell (Inrad) consisting of a 2-cm crystal of KD*P (KD_2PO_4) aligned with its principal axis along the beam direction. Application of about ±1000 V to the Pockels cell's electrodes results in $\pm\frac{1}{4}\lambda$ retardation. The voltage is pulsed to eliminate the effects of long-term relaxation in the retardation which occurs with a dc electric field, and a slow (100 μs) rise time is chosen to avoid crystal resonances. Initial alignment of the Pockels cell is made optically and final alignment makes use of the Stark effect in thallium itself (see Sec. IV C). The sign of helicity of the UV beam as a function of Pockels-cell polarity has been determined optically and by observation of the α-β interference in thallium [see Eq. (11)].

The 2.18-μm light is produced by a Chromatix CMX-4/IR optical parametric oscillator (OPO) driven by $L2$. The resonant wave in the OPO has $\lambda=800$ nm, and the difference wavelength is 2.18 μm with a bandwidth of 2 cm^{-1} (Chromatix specification) and a spectral profile with the same mode spacing as the pump (150 MHz). This is sufficient to saturate the $7\,^2P_{1/2}$-$8\,^2S_{1/2}$ transition, which has a Doppler width of 230 MHz. Typically we obtain 0.2–0.3 mJ/pulse, which is attenuated by 50% before entering the cell to maximize analyzing power. Frequency jitter causes 10–15% signal fluctuations per pulse. The 2.18-μm beam is split into two beams of equal intensity with a thin wafer of polished silicon. The two beams pass through individually adjustable linear polarizers (Polaroid HR plastic) and crystalline quartz quarter-wave plates (Virgo optics) set to produce beams of opposite helicity in the two interaction regions defined by intersection with the UV beam (see Fig. 3). The fractional difference between signals observed in these two regions is proportional to the polarization P_e and quite independent of pulse-to-pulse intensity fluctuations of the light beams. The quarter-wave plates are rotated automatically about their axis parallel to $\hat{x}$ once every 128 pulses to reverse the helicity in each region. The 2.18-μm beams are aligned perpendicular to the 293-nm beam to within 1°. A computer-controlled solenoid-actuated flag automatically blocks the 2.18-μm beam for background measurements.

The adjustable linear polarizers compensate for imperfections in the orientation of the quarter-wave plates. We monitor the signal size asymmetry,

$$\Gamma_{IR}^{1,2}=\frac{S_{1,2}(IR+)-S_{1,2}(IR-)}{S_{1,2}(IR+)+S_{1,2}(IR-)}\,,$$

where IR± refers to the helicity of the infrared light, and 1, 2 refers to regions. By adjusting the rotational orientation of the linear polarizers, Γ_{IR}^1 and Γ_{IR}^2 can be made equal and both $\leq10^{-3}$. Because the $7P$-$8S$ transition is heavily saturated, the asymmetry in the admixture of incorrect polarization when $\Gamma_{IR}=10^{-3}$ is only $\sim2\times10^{-5}$. This equalizes the analyzing power for IR+ and IR− in each region (although the analyzing power is different in the two regions). By direct measurement, the intensity ratio is

$$\frac{I(\text{unwanted helicity})}{I(\text{desired helicity})}=\begin{cases}0.001 \text{ in region 1.}\\ 0.0025 \text{ in region 2.}\end{cases}$$

The rough vacuum tank contains an off-axis rotating window in the front, through which the 293-nm beam enters. This is rotated from time to time by hand so that the UV beam enters through a clean portion of the window. The dielectric mirror at the rear of the tank is used to reflect the UV beam back through the cell. It is back-surfaced so that contaminants from the oven cannot damage the dielectric film. The mirror is mounted off-axis on a rotating seal to allow selection of locations on the mirror which are clean and have minimal birefringence. The reflected beam can be blocked automatically by a solenoid-actuated flag controlled by the computer.

Water-cooled magnetic field coils capable of producing ±8 G along the x (UV beam) direction are mounted inside the vacuum tank. These are used for diagnostic purposes (see Sec. IV G). Large-diameter coils outside the vacuum system are used to cancel the Earth's field and to generate a large magnetic field in the y direction for observation of the Hanle effect (see Sec. IV E).

Each interaction region is viewed by two photomultiplier tubes. The 323-nm fluorescence accompanying $8S_{1/2}$-$6P_{3/2}$ decay is collimated by 38-mm-diameter $f/1$ fused silica lenses inside the oven, passes through holes in the heat shields, and then through double quartz windows in the detector ports. These windows are cooled by a flowing filtered solution of Phthalic acid (6 g potassium acid phthalate per liter distilled H_2O). This solution is a liquid filter with a sharp low-

pass cutoff at about 310 nm.[21] Next in line is an interference filter at 323 nm (peak transmission 25–30%, FWHM 2.5 nm) which also contains a UG-11 infrared and visible blocking filter. Finally there is a spatial filter consisting of a 38-nm-diameter $f/1$ quartz lens and an aperture at the focus.

The photomultipliers are 9780 QB (EMI) with bialkali photocathodes and quartz windows. The anodes of the two tubes viewing each region are connected together and capacitively coupled to charge integrating preamplifiers. The output pulse is amplified, digitized, and sent to an LSI-11/2 computer.

No component introduces electronic or digitizing noise greater than 10^{-3} of the signal, per pulse. A typical signal at each photomultiplier cathode on the 0-1 resonance at a Stark field of 215 V/cm is 10^4 photoelectrons per pulse. The signal-to-background ratio for these conditions is about 10:1. Most of the background is due to scattering and fluorescence of 293-nm laser photons in the cell walls. The remainder arises from excitation during atom-atom collisions and miscellaneous small effects.

For linearly polarized UV light with polarization $\hat{\epsilon}$, only the $F=0$–$F'=0$ transition is allowed for $\hat{\epsilon}\|\vec{E}$, while for $\hat{\epsilon}\perp\vec{E}$, only the 0-1 transition can occur. This fact is used to monitor the frequency of the light. (Here we ignore the 1-1, 1-0 transitions which are separated from the 0-0, 0-1 transitions by about 21 GHz.) After the UV laser beam is reflected back through the main cell and rough vacuum tank, it suffers two 90° reflections from aluminum mirrors with orthogonal planes of incidence. The retardation effects of each reflection cancel, leaving the beam circularly polarized but traveling parallel to $-z$ (see Fig. 3). It then passes through a fixed quarter-wave plate

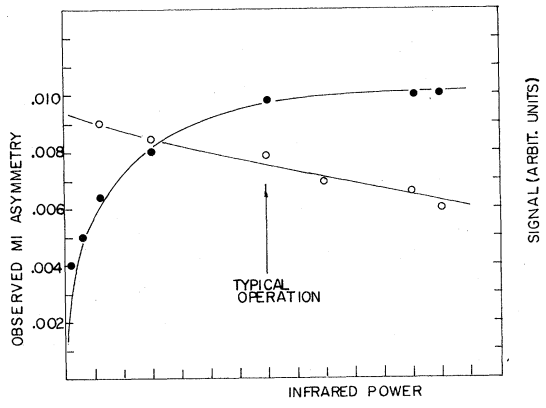

FIG. 5. ●: 323 nm fluorescent signal vs 2.18 μm intensity (right-hand scale). ○: Observed $M1$ asymmetry vs 2.18 μm intensity (left-hand scale).

which changes the ± helicity photons into alternative $\hat{\epsilon}_x$ or $\hat{\epsilon}_y$ linear polarizations. The beam enters a second vacuum tank which houses a separate oven and thallium cell with external electrodes. The fluorescence $(7\,^2P_{1/2}\rightarrow)\,7\,^2S_{1/2}\rightarrow 6\,^2P_{3/2}$ at 535 nm from this cell is viewed by a single phototube. Observation of the signal asymmetry between $I(\hat{\epsilon}_x)$ and $I(\hat{\epsilon}_y)$ determines the frequency directly in terms of the ratio $I(0\text{-}1)/I(0\text{-}0)$. This ratio, corrected for background dilution, is averaged over 256 pulses by the computer, which uses the result to tune $L1$. An intensity ratio $I(0\text{-}1)/I(0\text{-}0)=15$ is maintained in the monitor cell, which corresponds to the ratio $I(0\text{-}1)/I(0\text{-}0)=11$ in the main cell. The discrepancy is caused by higher efficiency for pumping $F=0$, $m_F=0$ $7\,^2P_{1/2}$ atoms to the $8\,^2S_{1/2}$ state, than for $F=1$, $m_F=\pm1$ atoms.

III. SELECTIVE EXCITATION AND ANALYZING POWER

The selective excitation of $7\,^2P_{1/2}$ atoms to the $8\,^2S_{1/2}$ state by 2.18 μm circularly polarized light may be calculated in a straightforward way using coupled rate equations for the eight Zeeman levels. The solution yields the signal size in the 323-nm channel, compared to the 535-nm signal which would be observed if all $7\,^2P_{1/2}$ atoms were allowed to decay via $7S$. The calculations also yield the polarization analyzing power at the frequencies where data are taken, vs 2.18-μm light intensity, and as a function of purity of 2.18-μm circular polarization. The effects of these can be seen in Fig. 5. As the infrared intensity increases, the 323-nm signal saturates. Further increase eventually causes a dilution in the measured polarization, due to imperfect 2.18-μm photon helicity.

The analyzing power has been measured by observing an interference between α and β Stark amplitudes in the 1-1 line. Excitation by circularly polarized UV produces a large polarization P_x of the $7\,^2P_{1/2}$ state along the $+x$ axis:

$$P_x(1\text{-}1)=\pm\frac{4\alpha\beta}{3\alpha^2+2\beta^2}\simeq\pm0.76 \qquad (11)$$

for ± 293-nm helicities, respectively. We have performed an experiment in which the 2.18-μm circularly polarized beam propagates along $-x$, opposite to the 293-nm beam. The 323-nm fluorescence exhibits a very large asymmetry depending on UV and IR helicities, arising from $P_x(1\text{-}1)$. As previously noted, observations of this asymmetry yield a measured analyzing power of 0.70 ±0.07, in agreement with calculations of selective excitation.

IV. ANALYSIS OF SYSTEMATIC ERRORS AND CORRECTIONS

A. General remarks

Certain important features of the apparatus and experimental procedure are utilized to reduce or eliminate possible systematic errors. They are as follows:

(a) All parity data are taken on the ($6\,^2P_{1/2}$, $F=0-7\,^2P_{1/2}$, $F'=1$) transition (0-1 line). The polarization for the 0-1 line is about 4.5 times greater than for the 1-1 line (although the total signal is about seven times less). More important, the 0-1 line is much less susceptible to possible systematic errors than the 1-1 line.

(b) Two interaction regions, with opposite IR circular polarizations, are used (as described in Sec. II).

(c) The electric-field polarity is reversed with each pulse.

(d) The sign of UV helicity, determined by Pockels-cell voltage polarity, is given by the sequence

$$+++--++--++--\cdots.$$

The sequence begins in a random place after each set of 128 pulses. It is chosen to eliminate correlations between E polarity and UV helicity.

(e) The IR circular polarization reverses after 128 pulses.

(f) The $7\,^2P_{1/2}$ polarization consists of a parity-nonconserving part $\mp 2\,\mathrm{Im}\mathcal{E}_P/\beta E$ and a parity-conserving part $-2\mathfrak{M}/\beta E$. The latter reverses with direction of UV beam and is largely canceled when the mirror is used. Data are taken with the mirror blocked, and with it unblocked. Background measurements (in which no IR reaches the interaction regions but other conditions are the same as for signal) also are taken with and without the mirror. Observations of the parity asymmetry are also carried out on the 0-0 line, as a null experiment.

As will be discussed in detail in Subsections C–G the remaining sources of possible systematic error not eliminated by these precautions are (1) imperfect UV circular polarization, (2) imperfectly aligned electric fields which do not reverse exactly in proportion to the main component of electric field, and (3) magnetic fields. It will be shown that these effects can be measured precisely by a combination of auxiliary experiments, and corrections applied with very small uncertainty.

B. Data collection

Three digitized signals are received from the computer on each pulse: one from each of the interaction regions (T_1, T_2), and one from the monitor cell. We have $T_{1,2}=S_{1,2}+B_{1,2}$, where S,B denote signal and background, respectively. The T_1, T_2 are compiled into 16 sums denoted by the array T_{ijkl}. Subscripts $ijkl$ are given by the following table:

$i=0,1$	UV pol $\pm$
$j=0,1$	E $\pm$
$k=0,1$	IR pol $\pm$
$l=1,2$	Region 1,2

After 256 pulses the T_{ijkl} are stored on disk. Eight polarizations P are computed by subtracting the regions:

$$P_{ijk}=\frac{T_{ijk1}-T_{ijk2}}{T_{ijk1}+T_{ijk2}}\,. \tag{12}$$

The following quantities are formed:

$$\Delta_M=\tfrac{1}{8}[(P_{000}-P_{001}-P_{010}+P_{011}+(P_{100}-P_{101}-P_{110}+P_{111})], \tag{13}$$

$$\Delta_P=\tfrac{1}{8}[(P_{000}-P_{001}-P_{010}+P_{011})-(P_{100}-P_{101}-P_{110}+P_{111})], \tag{14}$$

$$\Delta_E=\tfrac{1}{8}[(P_{000}-P_{001}+P_{010}-P_{011})-(P_{100}-P_{101}+P_{110}-P_{111})]. \tag{15}$$

Apart from background and residual systematic effects, to be discussed below, Δ_M is the polarization due to $M1$-Stark interference: $-2\mathfrak{M}/\beta E$, and Δ_P is the parity-nonconserving polarization $-2\,\mathrm{Im}(\mathcal{E}_P)/\beta E$. Δ_E and other signals and asymmetries calculated from the T_{ijkl} are used for diagnostic purposes and corrections to the data. The data collection sequence is discussed further in Sec. V A.

C. The effects of imperfect UV circular polarization

Various dilutions of the $M1$-Stark polarization occur because of background, small admixture of 0-0 intensity in the 0-1 line, and imperfection of the 2.18-μm polarization. In addition the $M1$-Stark interference depends on $\vec{k}$ and is thus reduced by reflections. If any of these dilutions vary as a function of UV circular polarization, this results in an UV-polarization-dependent observed $M1$ asymmetry which would be interpreted as a (false) parity asymmetry. However, the net effect can be expressed in terms of experimentally measured parameters.

The measured $M1$ asymmetry may be written as

$$\Delta_M=D_{\mathrm{IR}}\frac{S_f-S_r}{(S+B)}\,\Delta_{M0}\,, \tag{16}$$

where Δ_{M0} is the undiluted $M1$ asymmetry, D_{IR} is the IR analyzing power, and S_f, S_r are the signals in the 0-1 line for the forward and reflected UV beam, respectively. D_{IR} cancels in the ratio Δ_P/Δ_M so we ignore it in the following.

For data taken with the mirror blocked, it can then be shown that (16) becomes

$$\Delta_M = \frac{S_b}{(S+B)_b}\frac{1}{(f+1)}\frac{1-r}{1+r}\Delta_{M0}, \tag{17}$$

where $f = S_{00}/S_{01} \simeq 0.09$, r is the effective reflectance of the quartz cell, and b stands for "blocked data." The false parity asymmetry is then

$$\Delta_F = \frac{\Delta_{M+} - \Delta_{M-}}{2}, \tag{18}$$

where we employ $\Delta_{M\pm}$ for $\pm$ UV circular polarization. It can be shown that (18) becomes

$$\Delta_F^b = \Delta_{Mb}\left(\frac{1+f}{1-f}\right)\left[\frac{B_b}{S_b}(\Gamma_b - \gamma_b) + \frac{2f}{1+f}\Gamma_b\right], \tag{19}$$

where

$$\Gamma_b = \frac{(S+B)_{b+} - (S+B)_{b-}}{(S+B)_{b+} + (S+B)_{b-}}$$

and

$$\gamma_b = \frac{B_{b+} - B_{b-}}{B_{b+} + B_{b-}}.$$

The first term in (19) is due to asymmetric background dilutions, the second to 0-0 contamination. Each of the quantities on the right-hand side of (19) is measured during data collection. Fine adjustment of the Pockels-cell voltage is made during data collection to minimize Γ_b which is nonzero primarily because of polarization imperfections.

Most of our data were collected with the mirror unblocked. This was done to increase signal and reduce systematic effects associated with Δ_M (the latter is decreased by about a factor of 4 when the mirror is unblocked). However, the UV polarization does suffer a slight degradation on reflection from the mirror, which is back-surfaced, and this can also result in a difference S_f-S_r which depends on UV circular polarization. It can be shown that in the "unblocked" case,

$$\Delta_{Fu} = \Delta_{Mb}\left(\frac{1+f}{1-f}\right)\frac{(S+B)_b}{S_b(S+B)_u} \times \left[2(S+B)_b(\Gamma_b - \Gamma_u) + 2B_b(\Gamma_u - \gamma_b) + B_u(\gamma_u - \Gamma_u) + \frac{2f}{1+f}(2S_b - S_u)\gamma_u\right]. \tag{20}$$

The subscript u refers to "unblocked." The first term on the right-hand side of (20) accounts for forward- and reverse-beam polarization asymmetries. The other terms describe the dilutions already discussed; all are expressed in terms of measured quantities. It has been assumed in this discussion that the effective reflectance of the front and rear of the cell are the same.

D. The effects of misaligned electric fields

A static electric field of ±215 V/cm exists in each interaction region during each pulse. Ideally the field is along the y axis perpendicular to $\vec{k}$ (along $\hat{x}$) and $\hat{z}$ (the IR-beam direction). In reality $\vec{k}$ defines $\hat{x}$ and the 2.18-μm beam(s) define the $\hat{x}$-$\hat{z}$ plane. $\vec{E}$ may then have x, y, and z components, and $\vec{E}_+$, $\vec{E}_-$ may differ slightly in magnitude and direction.

We now analyze the consequences of this,[22] assuming the UV light is perfectly circularly polarized:

$$\hat{\epsilon}_\pm = \frac{\hat{y} \pm i\hat{z}}{\sqrt{2}}.$$

Assuming $\vec{E} = E_x\hat{x} + E_y\hat{y} + E_z\hat{z}$, a finite $7\,^2P_{1/2}$ polarization appears for the 0-1 transition even in the absence of $\mathfrak{M}$ and $\mathcal{E}_P$ amplitudes:

$$P_E = \mp\frac{2E_xE_z}{E_y^2} \quad \text{for } E_y^2 \gg E_x^2, E_z^2. \tag{21}$$

P_E reverses with UV circular polarization and behaves the same in this respect as Δ_P. However, if E reverses exactly P_E remains unchanged, unlike Δ_P. Therefore, P_E contributes a false parity asymmetry Δ_f only if $\vec{E}$ does not reverse exactly. We separate $\vec{E}$ into reversing and nonreversing components:

$$\vec{E}_+ = \vec{E}_0 + \overrightarrow{\Delta E}, \quad \vec{E}_- = -\vec{E}_0 + \overrightarrow{\Delta E}. \tag{22}$$

Assuming $E_{0y} \gg \Delta E_y, E_{0x}, \Delta E_x, E_{0z}, \Delta E_z$, we find

$$\Delta_f \simeq -\frac{(2E_{0x}\Delta E_z + 2E_{0z}\Delta E_x)}{E_{0y}^2} + \frac{4E_{0x}E_{0z}\Delta E_y}{E_{0y}^3}. \tag{23}$$

The quantities ΔE_y, E_{0x}, ΔE_x, E_{0z}, ΔE_z are determined experimentally (see subsection G).

E. Magnetic fields

Two magnetic field effects can contribute false parity asymmetries: hyperfine mixing and precession of $7\,^2P_{1/2}$ polarization components P_x, P_y into the z direction due to magnetic fields B_y, B_x, respectively (Hanle effect).

1. Hyperfine mixing

An external magnetic field mixes states of different m_F. We define the quantities

$$\omega_i^\eta = \frac{g_J\mu_0 B_i}{2h\Delta\nu_\eta}, \tag{24}$$

where $\Delta\nu_n$ is the hyperfine splitting of the $n\,^2P_{1/2}$ state. To lowest order in the magnetic field the 0-1 $7\,^2P_{1/2}$ polarization is

$$P = \mp \frac{2\mathfrak{M}}{\beta E}(\omega_x{}^6 - \omega_x{}^7)\frac{\alpha}{\beta}, \tag{25}$$

where E is assumed to be in the y direction. This polarization, like Δ_P, reverses with UV circular polarization and E. It yields a false parity asymmetry equal to that expected for Δ_P when $|B_x| = 5.5$ G. However, during the experiment $B_x \lesssim 0.01$ G, so this effect is small and we ignore it in the following discussion.

2. *Hanle effect*

The large polarization $P_x(1\text{-}1)$ along $\hat{x}$ for the 1-1 line [Eq. (11)] can be made to precess into the $\hat{z}$ axis by imposing a magnetic field B_y. With a separate apparatus we have observed the circular polarization of the 535-nm-decay fluorescence in the $\hat{z}$ direction, and thus have measured $A(7\,^2P_{1/2} \rightarrow 7\,^2S_{1/2})$ with results to be reported in a future publication. The precession can also be observed in 323-nm fluorescence, although this is complicated because of coupling of $7\,^2P_{1/2}$ and $8\,^2S_{1/2}$ states by the 2.18-μm circularly polarized laser field. The observations agree reasonably well with calculations of this effect. A measurement of the precession angle θ_x as a function of magnetic field B_x will be described in subsection G.

F. General treatment of systematic effects

We combine the aforementioned effects and write a general $6\,^2P_{1/2}(F=0) \rightarrow 7\,^2P_{1/2}(F'=1)$ transition amplitude for a thallium atom in arbitrary electric and magnetic fields. We also allow for imperfect UV circular polarization by writing the nominal $\pm$ polarization states as

$$\hat{R} = (1-\eta^2)^{1/2}\hat{\epsilon}_- + \eta e^{i\phi}\hat{\epsilon}_+, \tag{26}$$

$$\hat{L} = (1-\eta'^2)^{1/2}\hat{\epsilon}_+ + \eta' e^{i\phi'}\hat{\epsilon}_-, \tag{27}$$

respectively, and η, ϕ, η', ϕ' are arbitrary real numbers (but $\eta^2 \ll 1$, $\eta'^2 \ll 1$). We then obtain

$m_F' = 1$:

$$\begin{aligned} A_\pm = {} & \mp\frac{E_y\beta}{2}(1-Q_\pm) \mp \frac{iE_x\beta}{2}(1-Q_\pm) + \frac{iE_z\beta}{2}(1+Q_\pm) \pm \frac{\mathfrak{M}}{2}(1-Q_\pm) \\ & + \frac{\mathrm{Im}(\mathcal{E}_P)}{2}(1+Q_\pm) - \theta_x\frac{E_x\beta}{2}(1+Q_\pm) - i\theta_x\frac{\mathfrak{M}}{2}(1+Q_\pm) - i\theta_y\frac{E_x\beta}{2}(1+Q_\pm) + \frac{\theta_y\mathfrak{M}}{2}(1+Q_\pm) \\ & \pm\frac{i\theta_z E_y\beta}{2}(1-Q_\pm) \mp \frac{\theta_z E_x\beta}{2}(1-Q_\pm) + \frac{\theta_z E_z\beta}{2}(1+Q_\pm) \mp \frac{i\theta_z\mathfrak{M}}{2}(1-Q_\pm), \end{aligned} \tag{28}$$

$m_F' = 0$:

$$\begin{aligned} A_\pm = {} & \frac{-i}{\sqrt{2}}E_x\beta(1+Q_\pm) + \frac{\mathfrak{M}}{\sqrt{2}}(1+Q_\pm) \pm \frac{\mathrm{Im}(\mathcal{E}_P)}{\sqrt{2}}(1-Q_\pm) \\ & \mp\frac{\theta_x E_x\beta}{\sqrt{2}}(1-Q_\pm) \mp \frac{i\theta_x\mathfrak{M}}{\sqrt{2}}(1-Q_\pm) \pm \frac{\theta_y E_y\beta}{\sqrt{2}}(1-Q_\pm) - \frac{iE_z\beta\theta_y}{\sqrt{2}}\mathfrak{M}(1+Q_\pm), \end{aligned} \tag{29}$$

$m_F' = -1$:

$$\begin{aligned} A_\pm = {} & \pm\frac{E_y\beta}{2}(1-Q_\pm) \mp \frac{iE_x\beta}{2}(1-Q_\pm) - \frac{iE_z\beta}{2}(1+Q_\pm) \pm \frac{\mathfrak{M}}{2}(1-Q_\pm) \\ & + \frac{\mathrm{Im}(\mathcal{E}_P)}{2}(1+Q_\pm) - \frac{\theta_x E_x\beta}{2}(1+Q_\pm) - \frac{i\theta_x\mathfrak{M}}{2}(1+Q_\pm) + \frac{i\theta_y E_x\beta}{2}(1+Q_\pm) - \frac{\theta_y\mathfrak{M}}{2}(1+Q_\pm) \\ & \pm\frac{i\theta_z E_y\beta}{2}(1-Q_\pm) \pm \frac{\theta_z E_x\beta}{2}(1-Q_\pm) + \frac{\theta_z E_z\beta}{2}(1+Q_\pm) \pm \frac{i\theta_z\mathfrak{M}}{2}(1-Q_\pm). \end{aligned} \tag{30}$$

In these expressions $Q_+ = \eta e^{i\phi}$, $Q_- = \eta' e^{i\phi'}$, and θ_x, θ_y, θ_z are small Hanle rotations about the axes x, y, z, respectively. Also terms in η^2, η'^2, and terms involving hyperfine mixing, and of second order or higher in misalignment, have been omitted.

It may be shown that Eq. (28)–(30) result in the following contributions to the quantities Δ_M, Δ_P, and Δ_E defined by Eqs. (13), (14), and (15), respectively:

$$\begin{aligned} \Delta_M = {} & -\frac{2\mathfrak{M}}{\beta E_{0y}} + \frac{2\Delta E_x\theta_z}{E_{0y}} - \frac{2E_{0x}\Delta E_y\theta_z}{E_{0y}{}^2} + \frac{2\mathfrak{M}f(\alpha^2/\beta^2)(\eta\cos\phi + \eta'\cos\phi')}{E_{0y}\beta[1+f(\alpha^2/\beta^2)]^2} \\ & + \frac{2\theta_x\Delta E_y}{E_{0y}}(\eta\cos\phi - \eta'\cos\phi') - \frac{2\mathfrak{M}}{\beta E_{0y}}\left(\frac{E_{0z}}{E_{0y}} + \theta_x\right)(\eta\sin\phi - \eta'\sin\phi'), \end{aligned} \tag{31}$$

$$\Delta_P = -\frac{2\,\mathrm{Im}(\delta_P)}{\beta E_{0y}} - \frac{2E_{0x}\Delta E_z}{E_{0y}^2} + \frac{4E_{0x}\Delta E_y}{E_{0y}^2}\left(\frac{E_{0z}}{E_{0y}} - \theta_x\right) - \frac{2\Delta E_x}{E_{0y}}\left(\frac{E_{0z}}{E_{0y}} - \theta x\right)$$
$$- 2(\eta\sin\phi + \eta'\sin\phi')\left(\frac{\mathfrak{M}}{\beta E_{0y}}\right)\left(\theta_x + \frac{E_{0z}}{E_{0y}}\right) - \frac{4E_{0x}\mathfrak{M}\theta_y(\eta\sin\phi + \eta'\sin\phi')}{\beta E_{0y}^2}$$
$$+ \frac{2\mathfrak{M}f(\alpha^2/\beta^2)(\eta\cos\phi - \eta'\cos\phi')}{E_{0y}\beta[1+f(\alpha^2/\beta^2)]^2} + \frac{2\theta_x\Delta E_x}{E_{0y}}(\eta\cos\phi + \eta'\cos\phi'), \tag{32}$$

$$\Delta_E = -\frac{2E_{0z}E_{0x}}{E_{0y}^2} - \frac{2\Delta E_z\Delta E_x}{E_{0y}^2} + \frac{2\theta_x E_{0x}}{E_{0y}} - \frac{2\theta_x\Delta E_x\Delta E_y}{E_{0y}^2} - \left(\frac{2\Delta E_z\mathfrak{M}}{\beta E_{0y}^2}\right)(\eta\sin\phi + \eta'\sin\phi'). \tag{33}$$

In Eq. (32) the leading term gives true parity violation. The next three terms account for the effect of misaligned electric field; the last two of these are modified by the presence of a magnetic field in the x direction. Of the next two terms, proportional to $(\eta\sin\phi + \eta'\sin\phi')$, the first depends on E_{0z}/E_{0y} and is modified by the magnetic field B_x; the second is much smaller and may be ignored. The seventh term describes the 0-0 dilution effect already accounted for in the second term of Eq. (19) and the fourth term of Eq. (20) (subsection C). Finally, the eighth term in Eq. (32) is always very small during the experiment, and may be ignored. Thus, after the corrections embodied in Eq. (19) and (20) have been made and small terms have been ignored there remains the following false parity asymmetry:

$$\Delta_{\text{false}} = -\frac{2E_{0x}\Delta E_z}{E_{0y}^2} - \frac{2\Delta E_x}{E_{0y}}\left(\frac{E_{0z}}{E_{0y}} - \theta_x\right) + \frac{4E_{0x}\Delta E_y}{E_{0y}^2}\left(\frac{E_{0z}}{E_{0y}} - \theta_x\right) - \frac{2\mathfrak{M}}{E_{0y}\beta}\left(\frac{E_{0z}}{E_{0y}} + \theta_x\right)(\eta\sin\phi + \eta'\sin\phi'). \tag{34}$$

G. Methods of measuring false parity effects

We now describe independent measurements of E_{0x}, E_{0z}, ΔE_x, ΔE_z, ΔE_y, and $\eta\sin\phi + \eta'\sin\phi'$.

1. Information in parity data

ΔE_y: The total signal for each electric field direction, summed over regions and laser polarizations, is $S(E_\pm) \propto E_{0y}^2 \pm 2E_{0y}\Delta E_y$. We measure the asymmetry

$$\gamma_E \equiv \frac{S(E_+) - S(E_-)}{S(E_+) + S(E_-)} = \frac{2\Delta E_y}{E_{0y}}. \tag{35}$$

By adjustment of a resistor network in the E-field pulser, we maintain $\Delta E_y \lesssim 2\times 10^{-3} E_{0y}$.

2. Measurements with linearly polarized UV

ΔE_z: This can be measured using linearly polarized light at 45° with respect to the $\hat{y}$ axis. Let $\tilde{\epsilon}_\pm = (1/\sqrt{2})(\hat{y} \pm \hat{z})$. Then it can be shown that the signal sizes for the 0-1, 0-0 lines are as follows:

$$S_{01}(\tilde{\epsilon}_\pm) \propto \frac{\beta^2 E_y^2}{2}\left(1 \mp 2\frac{E_z}{E_y}\right), \tag{36}$$

$$S_{00}(\tilde{\epsilon}_\pm) \propto \frac{\alpha^2 E_y^2}{2}\left(1 \pm 2\frac{E_z}{E_y}\right), \tag{37}$$

respectively. Forming the experimental asymmetries

$$A(\tilde{\epsilon}_\pm) = \frac{S_{E+} - S_{E-}}{S_{E+} + S_{E-}},$$

where the subscripts $E_\pm$ refer to electric field orientation, we find

$$\frac{\Delta E_z}{E_{0y}} = \frac{1+f}{1-f}\,\frac{A(\tilde{\epsilon}_+) - A(\tilde{\epsilon}_-)}{4}. \tag{38}$$

E_{0z}/E_{0y}: The linear-polarization experiment provides additional information through Δ_P. With $\tilde{\epsilon}_\pm = (1/\sqrt{2})(\hat{y} \pm \hat{z})$, we obtain

$$\Delta_P = \frac{-2\mathfrak{M}}{\beta E_{0y}}\left(\theta_x + \frac{E_{0z}}{E_{0y}}\right) = \Delta_M\left(\theta_x + \frac{E_{0z}}{E_{0y}}\right), \tag{39}$$

where in (39) only the most significant terms have been retained. For $\theta_x = 0$, $E_{0z}/E_{0y} = \Delta_P/\Delta_M$. Since this formula applies to both blocked and unblocked data we may use a weighted average of the two results to obtain E_{0z}/E_{0y}. If we now employ a magnetic field $B_x = \pm 5$ G, it is possible to determine θ_x for these fields. The result is $\theta_x(5\text{ G}) = 0.22 \pm 0.01$, consistent with the rotation observed in the 1-1 line (subsection E).

3. Measurements employing magnetic fields and circularly polarized light

E_{0x}/E_{0y}: Returning to circular polarization but using the same magnetic fields we form the difference between $\Delta_E(+\theta_x)$ and $\Delta_E(-\theta_x)$ to eliminate terms independent of θ_x in Eq. (33). Keeping only the significant term we find

$$\frac{E_{0x}}{E_{0y}} = \frac{\Delta_E(+\theta_x) - \Delta_E(-\theta_x)}{4\theta_x}. \tag{40}$$

4. $\Delta E_x/E_{0y}$ and $(\eta\sin\phi + \eta'\sin\phi')$

Forming a similar difference for Δ_P one finds

$$\Delta_P(+\theta_x) - \Delta_P(-\theta_x) = 2\theta_x\left[\frac{2\Delta E_x}{E_{0y}} + \Delta_M(\eta\sin\phi + \eta'\sin\phi')\right]. \tag{41}$$

By comparing this difference for blocked and unblocked data one obtains

$$(\eta \sin\phi + \eta' \sin\phi') = \frac{[\Delta_{Pb}(+\theta) - \Delta_{Pb}(-\theta) - \Delta_{Pu}(+\theta) + \Delta_{Pu}(-\theta)]}{2\theta_x(\Delta_{Mb} - \Delta_{Mu})}, \quad (42)$$

$$\frac{\Delta E_x}{E_{0y}} = \frac{\Delta_{Pb}(-\theta) - \Delta_{Pb}(+\theta) - (\Delta_{Mb}/\Delta_{Mu})[\Delta_{Pu}(-\theta) - \Delta_{Pu}(+\theta)]}{2\theta_x(\Delta_{Mb}/\Delta_{Mu} - 1)}. \quad (43)$$

It should be noted that the interaction regions are defined by the intersections of the 293-nm and 2.18-μm laser beams and fill very small volumes. It is safe to assume that the quantities E_{0x}/E_{0y}, $\Delta E_x/E_{0y}$, etc., do not vary significantly from their average values in these volumes. Also, the measured E_{0x}/E_{0y}, $\Delta E_x/E_{0y}$, and $\eta \sin\phi + \eta' \sin\phi'$ are all diluted by the same polarization analyzing power as Δ_P, Δ_M, whereas E_{0z}/E_{0y} and $\Delta E_z/E_{0y}$ are not. As a result, the various products of these terms appearing in Δ_{false}[Eq. (34)] all have the same dilutions as Δ_P.

To summarize, all significant false parity asymmetries arising from Eqs. (28)–(30) have been measured by independent experiments.

V. DATA ANALYSIS AND RESULTS

A. Secondary data sets and auxiliary data

The sequence in which data are accumulated is shown in Table I(a). During one of these sets (which requires about 40 min) signal corrections [Eqs. (19) and (20)] and normalization are quite constant, since manual adjustments to the apparatus such as mirror rotation and balance of E field are generally done on a longer time scale.

We define a secondary data point as an average of 80 primary points (unblocked) and 48 primary points (blocked). One determines the average parity, $M1$ and signal asymmetries, and signal sizes necessary to perform the corrections of Eqs. (19) and (20). These corrections are calculated separately for each interaction region, averaged, and assigned a statistical uncertainty determined from the combined uncertainty of all the factors in Eqs. (19) and (20). The net correction is subtracted from $\Delta^i_{P,\text{obs}}$ to obtain Δ^i_P while the uncertainties are combined in quadrature. Each of the Δ^i_P and associated uncertainties are then normalized to $\Delta_{M,b} = 9.0 \times 10^{-3}$ to account for the variations in analyzing power between secondary data points which affect parity and $M1$ asymmetries in the same way. These variations are due to fluctuations in IR power and polarization, and changes in background and 0-0 dilution. A weighted average of the normalized Δ^i_P is then taken over a run (see Tables II and III).

It should be noted that the $M1$ data taken in the present experiment, when corrected for imperfect analyzing power, background, 0-0 dilution, and reflection effects, yield a result for $\mathfrak{M}$ in agreement with previous measurements.[15]

Interspersed throughout a run at intervals of approximately ten secondary data sets, are sets of auxiliary measurements needed to determine E_{0x}, E_{0z}, ΔE_x, ΔE_z, and $(\eta \sin\phi + \eta' \sin\phi')$. A typical sequence of auxiliary measurements is shown in Table I(b). In a typical run, there are about six such sequences. These measurements must also be corrected with Eqs. (19) and (20). In addition measurements with $B_x \neq 0$ must be corrected for hyperfine mixing and for reduction of Δ_M by rotation of the polarization away from the z axis. With these precautions E_{0x}, E_{0z}, ΔE_x, ΔE_z, and

TABLE I. Data accumulation sequences.

(a) Secondary parity data set
Circularly polarized UV, $B_x = 0$:

$uubuubu(B_uB_b)bubuubuubuubuubu(B_uB_b)bubuubuub$

(b) Calibration data
1. Circularly polarized UV, $B_x = \pm 5$ G:
$u\ b\ldots$(5 cycles) $(B_uB_b)u\ b\ldots$(5 cycles)
2. Linearly polarized UV, $B_x = 0$:
$ubub\ldots$(5 cycles) $(B_uB_b)ubub\ldots$(10 cycles) $(B_uB_b)ubub\ldots$(5 cycles)

u: signal+background, unblocked
b: signal+background, blocked
B_u: background, unblocked
B_b: background, blocked
Each symbol (e.g., u) represents four primary data points (see Sec. IV B) and a time of 1 min ($4 \times 256 = 1024$ pulses).

TABLE II. Parity data with Mirror ("unblocked") (Units of 10^{-7}).

	a	b	Systematic effects				g	
Run	Δ_p	Δ_p	c	d	e	f	Δ_p	Weight
1	261	159 ± 180	52 ± 47	14 ± 63	−10 ± 8	−3 ± 1	106 ± 197	2.564
2	91	195 ± 199	−1 ± 13	−30 ± 45	−27 ± 7	−1 ± 0	254 ± 205	2.379
3	−244	−103 ± 283	−13 ± 30	2 ± 30	−10 ± 9	0 ± 0	−82 ± 286	1.220
4	−141	−62 ± 146	10 ± 15	−30 ± 42	−21 ± 9	−1 ± 1	−20 ± 153	4.276
5	272	270 ± 179	9 ± 23	−22 ± 52	−61 ± 15	−1 ± 1	345 ± 188	2.817
6	−221	−171 ± 204	0 ± 3	2 ± 17	−8 ± 13	0 ± 1	−165 ± 205	2.376
7	192	49 ± 108	−6 ± 8	−25 ± 31	−12 ± 8	−1 ± 0	93 ± 113	7.841
8	22	124 ± 80	−2 ± 5	−11 ± 16	−69 ± 19	−1 ± 0	207 ± 84	14.201
9	−63	15 ± 197	15 ± 21	74 ± 109	−48 ± 19	1 ± 1	−27 ± 227	1.942
10	−141	160 ± 195	16 ± 25	−59 ± 73	−24 ± 12	−1 ± 1	228 ± 210	2.266
11	107	302 ± 136	−1 ± 13	−43 ± 51	−18 ± 10	−1 ± 1	365 ± 146	4.680
Average	46	103	4	−16	−36	−1	153 ± 45	

[a] Uncorrected.
[b] Signal correction included [Eq. (20)].
[c] $-(\eta \sin\phi + \eta' \sin\phi')2\mathfrak{M}/E_{0y}(E_{0z}/E_{0y})$.
[d] $-2E_{0z}\Delta E_x/E_{0y}^2$.
[e] $-2E_{0x}\Delta E_z/E_{0y}^2$.
[f] $+4E_{0x}E_{0z}\Delta E_y/E_{0y}^3$.
[g] Δ_p with all corrections.

$\eta \sin\phi + \eta' \sin\phi'$ can be extracted reliably and precisely.

Results of the auxiliary measurements are displayed by run in Table IV. Quantities $\Delta E_x, \Delta E_z$ are fairly constant from first to last run, although perhaps they show a slight increase with time (as the cell degraded gradually). The values of E_x and E_z also remain fairly constant except for deviations associated with adjustments of angles and positions of $L1$, $L2$ laser beams. The quantity $\eta \sin\phi + \eta' \sin\phi'$ varies more erratically from run to run, since it depends sensitively on Pockels-cell alignment, which was reset for each run. There is no indication of variation between realignments. The net contribution from this term averaged over all runs is small.

TABLE III. Parity data without mirror ("blocked") (Units of 10^{-7}).

	a	b	c	Systematic effects		f	g	
Run	Δ_p	Δ_P		d	e		Δ_P	Weight
1	194	180 ± 251	197 ± 179	14 ± 63	−12 ± 7	−3 ± 1	−16 ± 315	1.009
2	−50	−29 ± 247	−2 ± 47	−30 ± 45	−14 ± 7	0 ± 0	17 ± 256	1.532
3	508	542 ± 469	−47 ± 111	2 ± 30	−20 ± 11	0 ± 1	607 ± 483	0.429
4	451	434 ± 225	39 ± 58	−30 ± 42	−22 ± 12	−1 ± 0	448 ± 236	1.789
5	73	88 ± 324	28 ± 74	−22 ± 52	−35 ± 18	−1 ± 1	118 ± 337	0.881
6	−358	−362 ± 401	0 ± 8	3 ± 21	−15 ± 27	0 ± 1	−350 ± 403	0.617
7	23	12 ± 195	−30 ± 42	−25 ± 31	−8 ± 8	−1 ± 0	76 ± 202	2.450
8	130	159 ± 110	−7 ± 17	−11 ± 16	−56 ± 13	−1 ± 0	234 ± 113	7.804
9	86	76 ± 269	137 ± 191	74 ± 109	−53 ± 22	1 ± 1	−83 ± 348	0.825
10	−221	−185 ± 258	61 ± 99	−59 ± 73	−24 ± 10	−1 ± 1	−162 ± 286	1.223
11	133	155 ± 186	−5 ± 49	−43 ± 51	−21 ± 11	−1 ± 1	225 ± 199	2.518
Average	104	118	15	−18	−33	−1	155 ± 58	

[a] Uncorrected.
[b] Signal correction included [(Eq. (19)].
[c] $-(\eta \sin\phi + \eta' \sin\phi')2\mathfrak{M}/E_{0y}(E_{0z}/E_{0y})$.
[d] $-2E_{0z}\Delta E_x/E_{0y}^2$.
[e] $-2E_{0x}\Delta E_z/E_{0y}^2$.
[f] $+4E_{0x}E_{0z}\Delta E_y/E_{0y}^3$.
[g] Δ_p with all corrections.

TABLE IV. Results of auxiliary measurements.

Run	a	b	c	d	e	f	g
1	210 ± 102	103 ± 43	20 ± 2	22 ± 2	17 ± 11	22 ± 10	−5 ± 19
2	−2 ± 45	116 ± 42	20 ± 2	23 ± 2	48 ± 9	28 ± 12	10 ± 11
3	−99 ± 97	53 ± 73	19 ± 2	12 ± 2	32 ± 25	42 ± 17	−1 ± 20
4	80 ± 51	54 ± 45	26 ± 2	27 ± 2	30 ± 11	34 ± 16	22 ± 12
5	36 ± 69	86 ± 62	26 ± 2	28 ± 2	83 ± 14	51 ± 22	9 ± 16
6	1 ± 73	−12 ± 63	41 ± 3	41 ± 2	10 ± 16	16 ± 26	10 ± 18
7	−39 ± 35	85 ± 43	23 ± 1	22 ± 1	22 ± 12	14 ± 13	12 ± 8
8	−14 ± 27	51 ± 36	33 ± 2	33 ± 2	83 ± 19	67 ± 12	8 ± 6
9	−173 ± 69	−88 ± 87	26 ± 2	24 ± 2	70 ± 23	71 ± 24	29 ± 14
10	43 ± 53	158 ± 61	17 ± 2	21 ± 1	44 ± 18	54 ± 18	14 ± 12
11	−5 ± 42	124 ± 46	20 ± 1	22 ± 1	31 ± 15	40 ± 17	13 ± 10

[a] $(\eta \sin\phi + \eta' \sin\phi') \times 10^{-3}$.
[b] $10^{-4} E_{0x}/E_{0y}$.
[c] $10^{-4} (E_{0x}/E_{0y})_b$.
[d] $10^{-4} (E_{0x}/E_{0y})_u$
[e] $10^{-5} (\Delta E_x/E_{0y})_u$
[f] $10^{-5} (\Delta E_x/E_{0y})_b$
[g] $10^{-5} \Delta E_x/E_{0y}$.

B. Results

The normalized average corrections for a given run are subtracted from the weighted average of the normalized Δ_p^i. The statistical uncertainty associated with each correction is combined in quadrature with the statistical uncertainty in the normalized Δ_p^i, for this run. This, finally, is a measurement of the parity asymmetry with associated statistical uncertainty. Our total data sample consists of 11 such runs, listed in Tables II and III. A weighted average yields

$$\Delta_{Pb} = 1.55 \pm 0.58 \times 10^{-5}, \tag{44}$$

$$\Delta_{Pu} = 1.53 \pm 0.45 \times 10^{-5}. \tag{45}$$

The data were also treated by applying the field corrections to each secondary data point and then combining. The results of this method are very close to the values quoted.

C. Correlation tests

A correlation study was done on the set of 425 secondary data points, both before and after corrections were applied, to examine the possible dependence of Δ_p on other system parameters (see Table V). Before corrections one finds a high correlation between Δ_{Pu} and Γ_b-Γ_u [see Eq. (20)] as well as between Δ_{Pb} and Γ_b [see Eq. (19)]. The only significant correlation surviving after the corrections is between Δ_{Pu} and Γ_b-Γ_u, and it has reversed sign. This suggests that the correction of Eq. (20) has been overestimated (by about 30%). We believe that this is largely due to reflections in the cell, which can only be estimated crudely. Therefore, we average the results of our model [Eq. (20)] and the predictions of the correlation study, and expand the systematic error to include both possibilities. This lowers the average of Δ_{Pu} by 0.10×10^{-5} from that originally calculated. All other correlations with the corrected data are at an acceptably low level.

D. Systematic uncertainties and final results

The systematic uncertainties are summarized in Table VI. Since the sources of these systematic effects are uncorrelated, we combine the uncertainties in quadrature. The final results are

$$\Delta_{Pb} = (1.55 \pm 0.58 \pm 0.06) \times 10^{-5} \tag{46}$$

$$\Delta_{Pu} = (1.43 \pm 0.45 \pm 0.11) \times 10^{-5}, \tag{47}$$

where the first uncertainty in each equation is statistical and the second is systematic. Since these results are consistent they may be combined to yield the result

$$\Delta_P = (1.48 \pm 0.36 \pm 0.09) \times 10^{-5}. \tag{48}$$

The corrected result for data taken on the 0-0 line is $\Delta_{00} = -(0.13 \pm 0.82 \pm 0.02) \times 10^{-5}$, where no $7\,^2P_{1/2}$ polarization is expected.

In order to compare with theory we calculate $\delta = 2\,\mathrm{Im}\mathcal{E}_p/\mathfrak{M}$. We take the ratio $2\Delta_p(0\text{-}1)/\Delta_M'$ where $\Delta_M' = 9.0 \times 10^{-3} K$. The factor K corrects for reflections from the rear of the main cell, which reduces Δ_M but not Δ_P. We estimate $K = 1.17$, but it might be somewhat smaller, which leads to a skewness in our final result,

TABLE V. Correlation tests (see Sec. VC). Results for 425 secondary data points (defined in Sec. VA). Subscript r indicates uncorrected; s indicates corrected.

x	y	R	P
$\Delta_{Pu,r}$	t	0.039	0.42
$\Delta_{Pu,s}$	t	−0.019	0.70
$\Delta_{Pb,r}$	t	−0.014	0.77
$\Delta_{Pb,s}$	t	−0.014	0.77
$\Delta_{Pu,r}$	$\Gamma_b-\Gamma_u$	0.239	6.5×10^{-7}
$\Delta_{Pu,s}$	$\Gamma_b-\Gamma_u$	−0.103	3.4×10^{-2}
$\Delta_{Pb,r}$	Γ_b	0.109	2.5×10^{-2}
$\Delta_{Pb,s}$	Γ_b	0.048	0.32
$\Delta_{Pu,r}$	$\Gamma_{u1}-\Gamma_{u2}$	0.019	0.70
$\Delta_{Pb,s}$	$\Gamma_{u1}-\Gamma_{u2}$	−0.006	0.90
$\Delta_{Pu,s}$	$\Delta_{E,u}$	0.036	0.46
$\Delta_{Pb,s}$	$\Delta_{E,b}$	−0.058	0.23
$\Delta_{Pu,r}$	Γ_u	0.042	0.39
$\Delta_{Pu,s}$	Γ_u	−0.046	0.34
$\Delta_{Pu,s}$	$\Delta_{Pb,s}$	−0.025	0.61
$\Delta_{Pu,r}$	$\sigma_{u,r}$	0.039	0.42
$\Delta_{Pu,s}$	$\sigma_{u,s}$	0.000	1.0
$\Delta_{Pb,r}$	$\sigma_{b,r}$	0.089	6.7×10^{-2}
$\Delta_{Pb,s}$	$\sigma_{b,s}$	0.066	0.17
$\Delta_{Pu,r}$	Δ_{Mb}	0.026	0.59
$\Delta_{Pu,s}$	Δ_{Mb}	0.041	0.40
$\Delta_{Pb,r}$	Δ_{Mb}	0.003	0.95
$\Delta_{Pb,s}$	Δ_{Mb}	0.028	0.56
σ_M	Δ_{Mb}	−0.041	0.40

$$R=\frac{\sum_i 1/\sigma_i^2\sum_i x_i y_i/\sigma_i^2-\left(\sum_i x_i/\sigma_i^2\right)\left(\sum_i y_i/\sigma_i^2\right)}{\{[\sum 1/\sigma_i^2\sum x_i^2/\sigma_i^2-(\sum x_i/\sigma_i^2)^2][\sum 1/\sigma_i^2\sum y^2{}_i/\sigma_i^2-(\sum y_i/\sigma_i^2)^2]\}^{1/2}}$$

P = probability that the two data sets come from uncorrelated parent populations. t = "time" correlation = correlations between successive secondary data points.

TABLE VI. Systematic uncertainties.

Source	Possible contribution to Δ_{Pb}	Δ_{Pb}
Uncorrected signal asymmetries	$<2\times10^{-8}$	$<2\times10^{-8}$
Hyperfine mixing	$<4\times10^{-8}$	$<1\times10^{-8}$
E-UV correlation	$<1\times10^{-7}$	$<3\times10^{-8}$
E_z (imperfect cancellation of residual B_x)	$<4\times10^{-7}$	$<3\times10^{-7}$
ΔE_z (imperfect UV, E subtraction)	$<4\times10^{-7}$	$<4\times10^{-7}$
E_x (misaligned B_x and possible admixture of 1-1 line)	$<7\times10^{-8}$	$<7\times10^{-8}$
ΔE_x (failure of approximation that effect is same with and without mirror)	$<1\times10^{-7}$	$<1\times10^{-7}$
Same as previous item for $\eta\sin\phi+\eta'\sin\phi'$	$<1\times10^{-7}$	$<3\times10^{-8}$
Signal corrections[a]	$<2\times10^{-7}$	$<1\times10^{-6}$
Totals combined in quadrature	$<6\times10^{-7}$	$<1.1\times10^{-6}$
Dilution due to UV-polarization imperfection[b]	$<2\times10^{-7}$	$<2\times10^{-7}$

[a] See Sec. VC.
[b] This effect can only reduce the observed asymmetry.

$$\delta = (2.8 \pm 0.7^{+0.3}_{-0.2}) \times 10^{-3} . \quad (49)$$

This result is consistent with theory [see Eq. (5)].

VI. CONCLUSIONS

The result (49) may be expressed in terms of Q_W, which is defined as

$$Q_W^S = Z(1 - 4\sin^2\theta_W) - N$$

in the standard model, and takes the values $Q_W^S(^{205}\mathrm{Tl}) = -117.5$, $Q_W^S(^{203}\mathrm{Tl}) = -115.5$ for $\sin^2\theta_W = 0.23$. We find

$$Q_{W,\mathrm{expt}}(\mathrm{Tl}) = -155 \pm 63 , \quad (50)$$

where the uncertainty includes that in $(\mathcal{E}_p)_{\mathrm{theo}}$ as well as the uncertainty in δ_{expt}.

The results of electron-scattering and atomic-physics experiments in Tl and Bi may be combined with neutrino-nucleon and neutrino-electron scattering data to provide a stringent test of neutral weak-interaction theories. In carrying out this analysis it is useful to employ the simplest model-independent assumptions, as was done by Hung and Sakurai.[23] They show that if one merely assumes μe universality, that the contributions of heavy quarks, c, s, ... may be neglected, and that all neutral weak currents possess only V and A components, then the theory is characterized by ten coupling constants $\tilde{\alpha}$, $\tilde{\beta}$, $\tilde{\gamma}$, $\tilde{\delta}$, α, β, γ, δ, g_V, and g_A, which must be determined by experiment. The neutrino-nucleon scattering data completely determine α, β, γ, and δ (up to an overall sign ambiguity), while neutrino-electron scattering results determine g_V, g_A up to a (twofold) V,A ambiguity. The polarized-electron-scattering experiment[7,8] yields

$$\tilde{\alpha} + \tfrac{1}{3}\tilde{\gamma} = -0.60 \pm 0.16, \quad \tilde{\beta} + \tfrac{1}{3}\tilde{\delta} = 0.31 \pm 0.51 . \quad (51)$$

The heavy atom experiments are sensitive to an almost orthogonal linear combination of $\tilde{\alpha}$ and $\tilde{\gamma}$:

$$Q_W(\mathrm{T}) = 42\tilde{\alpha} - 612\tilde{\gamma} . \quad (52)$$

As Hung and Sakurai have noted, further restrictions on the coupling constants are obtained if one assumes the "factorization" hypothesis. Employing result (50), formula (52), and factorization we represent the resulting constraints on $\tilde{\alpha}$ and $\tilde{\gamma}$ in Fig. 6 and obtain

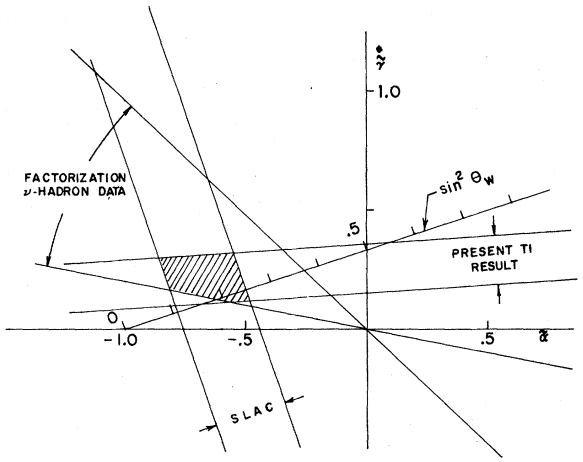

FIG. 6. Constraints on $\tilde{\alpha}, \tilde{\gamma}$ from: ν-hadron scattering (factorization hypothesis); SLAC polarized electron experiment; results of the present Tl experiment. The region of the $\tilde{\alpha}, \tilde{\gamma}$ plane consistent with all of these constraints is cross hatched.

$$\tilde{\alpha} = -0.67 \pm 0.16 , \quad (53)$$

$$\tilde{\gamma} = +0.18 \pm 0.06 . \quad (54)$$

Assuming factorization, Hung and Sakurai show that all ten constants are determined without ambiguities and are in excellent agreement with predictions of the standard model for $\sin^2\theta_W = 0.23$. Without factorization $\tilde{\beta}$ and $\tilde{\delta}$ remain undetermined experimentally.

A substantial improvement in the measurement of $\mathrm{Im}(\mathcal{E}_p)/\beta$ for the $6\,^2P_{1/2}$-$7\,^2P_{1/2}$ transition in Tl seems possible by means of a technique utilizing linearly polarized 293-nm light and an external magnetic field. This experiment is being pursued in our laboratory.

ACKNOWLEDGMENTS

We thank S. Chu and R. Conti for invaluable contributions to the early phases of the experiment, and D. Neuffer for calculations. We are grateful to P. Drell for many discussions and useful assistance, and glassblowers D. Anderberg and R. Hamilton for excellent workmanship. This research was done under the auspices of the Chemical Sciences Division, Office of Basic Energy Sciences, U.S. Department of Energy.

[1] S. Weinberg, Phys. Rev. Lett. 19, 1264 (1967).
[2] A. Salam, in *Elementary Particle Physics: Relativistic Groups and Analyticity (Nobel Symposium No. 8)*, edited by N. Svartholm (Almqvist & Wiksell, Stockholm, 1968), p. 367.
[3] M. A. Bouchiat and C. Bouchiat, Phys. Lett. 48B, 111 (1974).
[4] M. A. Bouchiat and C. Bouchiat, J. Phys. (Paris) 35, 899 (1974).
[5] M. A. Bouchiat and C. Bouchiat, J. Phys. (Paris) 36,

493 (1975).
[6]E. D. Commins and P. H. Bucksbaum, Annu. Rev. Nucl. Part. Sci. 30, 1 (1980).
[7]C. Y. Prescott *et al.*, Phys. Lett. 77B, 347 (1978).
[8]C. Y. Prescott *et al.*, Phys. Lett. 84B, 524 (1979).
[9]L. M. Barkov and M. S. Zolotorev, Pis'ma Zh. Eksp. Teor. Fiz. 28, 544 (1978) [(JETP Lett. 28, 503 (1978)].
[10]L. M. Barkov and M. S. Zolotorev, Phys. Lett. 85B, 308 (1979).
[11]J. H. Hollister *et al.*, Phys. Rev. Lett. 46, 643 (1981).
[12]Y. V. Bogdanov *et al.*, Report No. 43, 1980, Quantum Physics Institute, P. N. Lebedev Institute, Academy of Science, USSR, Moscow (unpublished).
[13]R. Conti *et al.*, Phys. Rev. Lett. 42, 343 (1979).
[14]P. Bucksbaum, E. Commins, and L. Hunter, Phys. Rev. Lett. 46, 640 (1981).
[15]S. Chu, E. Commins, and R. Conti, Phys. Lett. 60A, 96 (1977).
[16]V. N. Novikov, O. P. Sushkov, and I. B. Khriplovich, Zh. Eksp. Teor. Fiz. 71, 1665 (1976) [Sov. Phys.—JETP 44, 872 (1976)].
[17]D. Neuffer and E. D. Commins, Phys. Rev. A 16, 844 (1977).
[18]B. P. Das, J. Andriessen, S. N. Ray, Mina Vajed-Samii, and T. P. Das (unpublished).
[19]A. Flusberg, T. Mossberg, and S. Hartmann, Phys. Rev. A 14, 2146 (1976).
[20]S. Chu and R. W. Smith, Opt. Commun. 28, 221 (1979).
[21]M. Kasha, J. Opt. Soc. Am. 38, 929 (1948).
[22]M. A. Bouchiat, J. Guená, and L. Pottier, J. Phys. Lett. (Paris) 41, L-299 (1980).
[23]P. Q. Hung and J. J. Sakurai, Phys. Lett. 88B, 91 (1979).